

1 Improved RepVGG Ground-Based Cloud Image Classification 2 with Attention Convolution

3 Chaojun Shi^{1, 2}, Leile Han¹, Ke Zhang^{1, 2}, Hongyin Xiang^{1, 2}, Xingkuan Li¹, Zibo Su¹, and Xian
4 Zheng¹

5 ¹Department of Electronic and Communication Engineering, North China Electric Power University, Baoding 071003,
6 China

7 ²Hebei Key Laboratory of Power Internet of Things Technology, North China Electric Power University, Baoding
8 Hebei 071003, China

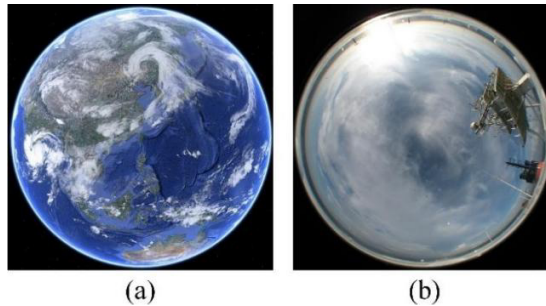
9 *Correspondence to:* Chaojun Shi (scj@ncepu.edu.cn) and Hongyin Xiang (66283880@qq.com)

10 **Abstract.** Atmospheric clouds greatly impact the Earth’s radiation prediction, hydrological cycle, and climate change.
11 Accurate automatic recognition of cloud shape based on ground-based cloud image is helpful to analyze solar
12 irradiance, water vapor content, and atmospheric motion, and then predict photovoltaic power, weather trends, and
13 severe weather changes. However, the appearance of clouds is changeable and diverse, and its classification is still
14 challenging. In recent years, convolution neural network (CNN) has made great achievements in ground-based cloud
15 image classification. However, traditional CNNs poorly associate long-distance clouds, making the extraction of
16 global features of cloud images quite problematic. This study attempts to mitigate this problem by elaborating a
17 ground-based cloud image classification method based on the improved RepVGG convolution neural network and
18 attention mechanism. Firstly, the proposed method increases the RepVGG residual branch and obtains more local
19 detail features of cloud images through small convolution kernels. Secondly, an improved channel attention module
20 is embedded after the residual branch fusion, effectively extracting the global features of cloud images. Finally, the
21 linear classifier is used to classify the ground cloud images. Finally, the warm-up method is applied to optimize the
22 learning rate in the training stage of the proposed method, making it lightweight in the inference stage and thus
23 avoiding overfitting and accelerating the model’s convergence. The proposed method is validated on MGCD and
24 GRSCD ground-based cloud image datasets, with the respective classification accuracy values of 98.15 and 98.07%,
25 outperforming those of ten most advanced methods used as the reference. The results obtained are considered
26 instrumental in ground-based cloud image classification.

27 1. Introduction

28 In meteorology, cloud is an aerosol consisting of a visible mass of water droplets, ice crystals, their aggregates or
29 other particles suspended in the atmosphere. Clouds of different types cover over 70% of the Earth surface (Qu et al.,
30 2021; Gyasi and Swarnalatha, 2023; Fabel et al., 2022). Cloud analysis plays a crucial role in meteorological

31 observation because clouds can affect the Earth's water cycle, climate change, and solar irradiance (Gorodetskaya et
32 al., 2015; Goren et al., 2018; Zheng et al., 2019). Cloud observation methods mainly include satellite observation
33 (Norris et al., 2016; Zhong et al., 2017; Li et al., 2023) and ground observation (Calbó and Sabburg, 2008; Nouri et
34 al., 2019; Lin et al., 2023). Satellite observation refers to the distribution, movement, and change of clouds observed
35 by high-resolution remote sensing satellites from the perspective of the outside to the inside. When observing local
36 sky areas, its decimeter-level observation performance cannot obtain a sufficient resolution to describe the
37 characteristics of different clouds blending in detail (Long et al., 2023; Sarukkai et al., 2020). Compared with satellite
38 observation, ground-based observation opens up a new way to monitor and understand regional sky conditions. Its
39 equipment can not only observe local sky areas but also capture ground-based cloud images with higher resolution.
40 The observation effect is shown in Figure 1.



41
42 **Figure 1: Satellite cloud and Ground-based cloud observation images: (a) Satellite cloud image. The picture is from the**
43 **National Satellite Meteorological Center: <http://www.nsmc.org.cn/>; (b) Ground-based cloud image (Johnson et al., 1989).**

44 Typical ground-based cloud observation instruments include All-Sky Imager (ASI) (Shi et al., 2019; Cazorla et al.,
45 2008), Total Sky Imager (TSI) (Johnson et al., 1989; Tang et al., 2021), etc. The relevant equipment and ground-based
46 cloud images are shown in Figure 2.



47
48 **Figure 2: Two kinds of ground-based cloud images and their observation equipment: (a) TSI ground-based cloud image**
49 **and its observation equipment (Johnson et al., 1989); (b) ASI ground-based cloud image and its observation**
50 **equipment (Cazorla et al., 2008).**

51 Ground-based cloud observation can obtain more obvious cloud characteristics by observing the information at the
52 bottom of the cloud, which is conducive to assisting the prediction of local photovoltaic power generation. Clouds
53 play an important role in maintaining the atmospheric radiation budget balance by suppressing short-wave and long-

54 wave solar radiation (Taravat et al., 2015). Pv power prediction is affected by multiple factors such as cloud genus,
55 cloud cover change, solar irradiance, and solar cell performance in local areas, among which cloud genus is an
56 important factor affecting PV power prediction (Zhu et al., 2022). Therefore, it is of great significance to accurately
57 obtain sky cloud information through cloud observation and then accurately classify clouds for accurate prediction of
58 photovoltaic power generation (Alonso-Montesinos et al., 2016). The traditional ground-based cloud observation
59 method is mainly manual observation, which relies heavily on the experience of observers, cannot achieve
60 standardization, and has low efficiency. Therefore, ground-based cloud automatic observation has been widely
61 concerned by scholars. In recent years, with the development of digital image acquisition devices, many ground-based
62 whole-sky cloud image acquisition devices have emerged at home and abroad, providing massive data support for
63 automatic ground-based cloud observation (Pfister et al., 2003).

64 Ground-based cloud image classification is an important part of the foundation of automatic cloud observation and
65 is the key to climate change and photovoltaic power prediction. The classification of ground-based cloud images
66 mainly classifies each cloud image taken from the ground into the corresponding cloud genus by extracting cloud
67 image features, such as cirrus, cumulus, stratus, stratus nimbus, etc. According to different cloud image feature
68 extraction methods, the ground-based cloud image classification method is divided into based on traditional machine
69 learning method and based on deep learning method (Hu et al., 2018). Most of the ground-based cloud image
70 classification methods based on traditional machine learning classify cloud images by artificially designing cloud
71 image features, while the ground-based cloud image classification methods based on deep learning mainly classify
72 cloud images through self-learning cloud image features of deep neural network (DNN) (Wu et al., 2019).

73 Early ground-based cloud image classification studies relied on manual classification methods, which focused on
74 features such as texture, structure, and color, combined with traditional machine learning methods to classify ground-
75 based cloud images. These methods include a decision tree, K-nearest neighbor (KNN) classifier, support vector
76 machine (SVM), etc. (Singh and Glennen, 2005) proposed a method for automatically training the texture function of
77 a cloud classifier. In this method, five feature extraction methods including autocorrelation, co-occurrence matrix,
78 edge frequency, Laws texture analysis, and original length are used respectively. Compared with other cloud
79 classification methods, this method has the advantages of high accuracy and fast classification speed, but its
80 classification ability for mixed clouds is insufficient. (Heinle et al., 2010) described cloud images by using spectral
81 features (mean value, standard deviation, skewness, and difference) and texture features (energy, entropy, contrast,
82 homogeneity, and cloud cover), and combined with a KNN classifier, divided ground cloud images into seven
83 categories. In addition, (Zhuo et al., 2014) reported that the spatial distribution of contour lines could represent the
84 structural information of cloud shapes, used the central description pyramid to simultaneously extract the texture and
85 structural features of ground-based cloud images, and used SVM and KNN to classify cloud images. It can be seen
86 that the traditional classification method of ground-based cloud images based on machine learning mainly uses hand-
87 designed texture, structure, color, shape, and other features to extract, and obtains high-dimensional feature expression

88 of ground-based cloud images through single feature or fusion feature. Traditional machine learning methods mostly
89 describe the features from the perspective of digital signal analysis and mathematical statistics, but ignore the
90 representation and interpretation of the visual features of the cloud image itself.

91 In recent years, under the background of cross-integration of different disciplines and artificial intelligence, the
92 ground-based cloud image classification method based on deep learning has become a research hotspot with its
93 superior classification performance. Aiming at the unique characteristics of ground-based cloud images, (Shi et al.,
94 2017) proposed Deep Convolutional Activations-Based Features (DCAFs) to classify ground-based cloud images,
95 and the results are better than the artificially designed cloud image features. Alternatively, (Ye et al., 2017) used CNN
96 to extract cloud image features and proposed a local pattern mining method based on ground-based cloud images to
97 optimize the local features of cloud images and improve the classification accuracy of cloud images. Zhang et al.
98 (2018a) put the wake cloud as a new genus of cloud into the ground-based cloud image database for the first time,
99 proposed a ground-based cloud image classification method based on CloudNet, and improved the classification
100 accuracy of the ground-based cloud images. More recently, (Wang et al., 2020) proposed an improved CloudA
101 network based on AlexNet. The classification accuracy on the Singapore Whole-Sky Imaging Categories (SWIMCAT)
102 ground-based cloud image dataset exceeded the traditional ground-based cloud image classification methods. Liu et
103 al. (2020b) proposed Multi-Evidence and Multi-Modal Fusion Networks (MMFN) by fusing heterogeneous features,
104 local visual features, and multi-mode information, which significantly improves the classification accuracy of cloud
105 images. Aiming at the problem that the traditional neural network has insufficient ability to classify the ground-based
106 cloud images within and between genera, (Zhu et al., 2022) proposed to use of an improved combined convolutional
107 neural network to classify the cloud images, and the classification accuracy is greatly improved compared with the
108 traditional neural network. Alternatively, (Yu et al., 2021) used two sub-convolutional neural networks to extract
109 features of ground-based cloud images and used weighted sparse representation coding to classify them, which solved
110 the problem of occlusion in multi-mode ground-based cloud image data and greatly improved the robustness of cloud
111 images classification. Liu et al. (2020a) introduced a ground-based cloud image classification method based on a
112 graph convolution network (GCN). However, the weight assigned by GCN failed to accurately reflect the importance
113 of connection nodes, thus reducing the discrimination of aggregated cloud image features. To make up for this
114 deficiency,(Liu et al., 2022) proposed a context attention network for ground-based cloud classification and publicly
115 released a new cloud classification dataset. In addition, Liu et al. (2020c) further combined CNN and GCN to propose
116 a multimodal ground-based cloud image classification method based on heterogeneous deep feature learning.
117 Alternatively, (Wang et al., 2021) elaborated a ground-based cloud image classification method based on Transfer
118 Convolutional Neural Network (TCNN) by combining deep learning and transfer learning. (Li et al., 2022) further
119 enhanced the classification performance of ground-based cloud images based on the improved Vision Transformer
120 combined with the EfficientNet-CNN. Being based on deep learning, this classification method significantly
121 outperformed the traditional machine learning methods.

122 CNN plays an important role in the field of target detection, image classification, and image segmentation,
123 especially in the tasks of power line fault detection (Zhao et al., 2016), face recognition (Meng et al., 2021), and
124 medical image segmentation (Zhang et al., 2021), and has been widely used and achieved great achievements. Ground-
125 based cloud image classification is an emerging task in the field of image classification and has achieved rapid and
126 considerable development based on the CNN method. However, it still has some shortcomings such as shallow
127 network level of ground-based cloud image classification method, limited ground-based cloud image classification
128 performance, and small ground-based cloud image classification dataset, which cannot verify the generalization ability
129 of large-scale ground-based cloud image classification dataset.

130 To solve the above problems, the current study improved the RepVGG (Ding et al., 2021) and used it as a basis for
131 elaborating a new classification method for ground-based cloud images called CloudRVE (Cloud Representative
132 Volume Element Network). In this method, the ground-based cloud image was incorporated into the CNN model, and
133 its image features were extracted. Multi-branch convolution layer and channel attention module were used to capture
134 local and global features of the cloud image simultaneously time to enhance the classification performance of ground-
135 based cloud images. The method's application to the multi-modal ground-based cloud dataset named MGCD (Liu et
136 al., 2020a) and ground-based remote sensing cloud database (GRSCD) (Liu et al., 2020b) proved its superiority over
137 several state-of-the-art subsoil cloud image classification methods. The main contributions of this paper are as follows:

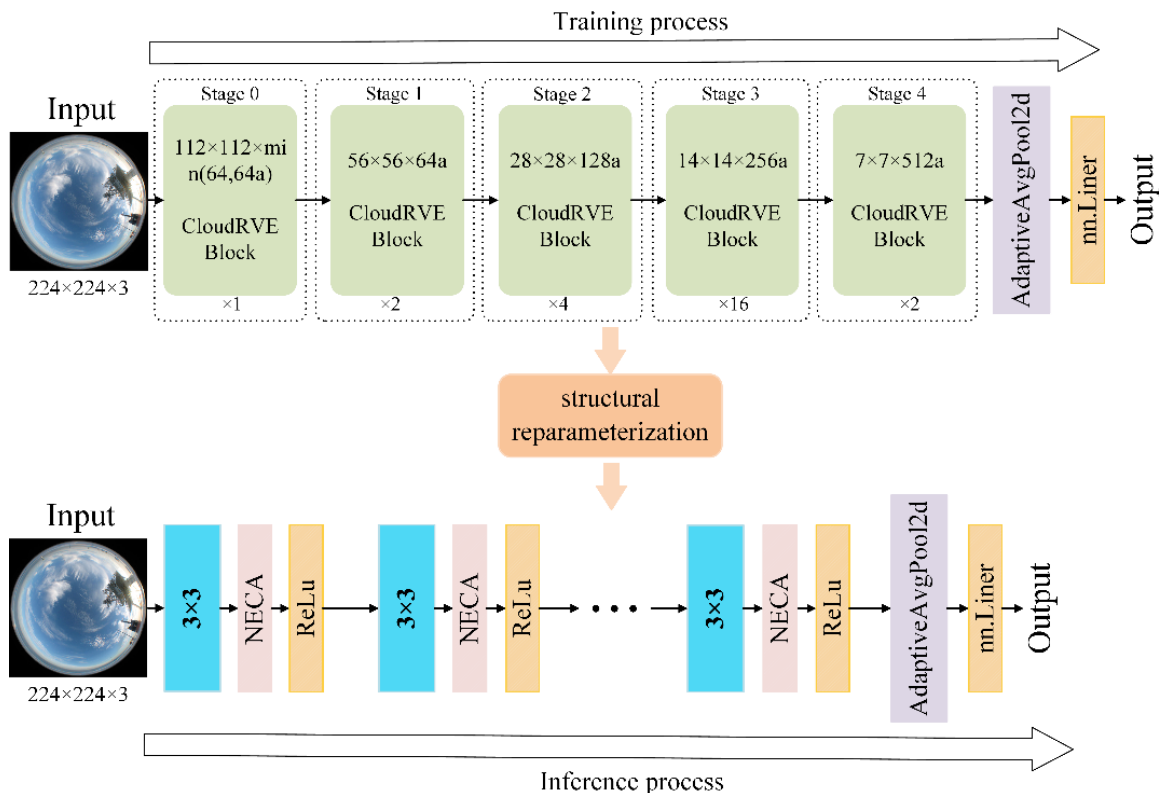
- 138 (1) This study elaborated the Improved RepVGG ground-based cloud image classification method with attention
139 convolution called CloudRVE. It broadened the residual structure and comprehensively combined the attention
140 mechanism's abilities to extract the cloud image's global features and describe in detail its local features in the
141 classification process.
- 142 (2) In particular, the Efficient Channel Attention network (ECA) was improved and incorporated into the feature
143 extraction process of ground-based cloud images, which optimization occurred through local cross-channel
144 interaction without dimensionality reduction. Besides, the structural re-parameterization in the inference stage
145 was performed, reducing the model complexity, improving the feature extraction performance, and enhancing
146 the network's learning ability of ground-based cloud image features.
- 147 (3) The comparative analysis of experimental results on the ground-based cloud image classification dataset MGCD
148 proved that the proposed method outperformed ten other state-of-the-art methods in classification accuracy. Its
149 application to GRSCD dataset further verified its generalization ability. Finally, the proposed method's training
150 process optimization and dynamical adjustment of its learning rate were provided by the warm-up method, and
151 the respective recommendations were drawn.

152 The rest of this paper is organized as follows. Section 2 elaborates on the structure and composition of the proposed
153 CloudRVE method for classifying ground cloud images. Section 3 briefly introduces the ground cloud image
154 classification datasets used in this paper and the model evaluation indices. Section 4 provides the experimental results

155 and discusses the feasibility and effectiveness of the proposed method. Finally, Section 5 concludes the study and
 156 outlines future research directions and practical application of the research results.

157 2. Methods

158 2.1 Overview of Method



159
 160 **Figure 3: CloudRVE network framework. Ground-based cloud images come from Kiel-F datasets (Kalisch and Macke,**
 161 **2008).**

162 This section shows the overall architecture of the proposed RepVGG-based improved classification method, as shown
 163 in Figure 3. In the CloudRVE training process, CloudRVE Block with a multi-branch topology structure is used to
 164 extract features of ground-based cloud images. The multi-branch topology structure has rich gradient information and
 165 a complex network structure, which can effectively improve the characterization ability of local feature information
 166 of ground-based cloud images. Feature maps extracted by CloudRVE Block enter the New Efficient Channel Attention
 167 (NECA) network and learn the feature relationships between sequences to obtain the global feature representation of
 168 an image. In addition, the warm-up method is incorporated into the CloudRVE training process to dynamically
 169 optimize the learning rate and accelerate the model parameter convergence to enhance the model training effect.

170 CloudRVE inference process uses the single branch topology structure of VGG-style (Simonyan and Zisserman, 2015),
 171 and through structural re-parameterization, the multi-branch convolutional layer and batch normalization (BN) (Ioffe
 172 and Szegedy, 2015) are converted into a 3×3 convolutional layer, increasing its inference speed. The CloudRVE
 173 training process and inference process use the linear classifier to classify the ground-based cloud images to get the
 174 final result. The specific framework parameter information of the model is shown in Table 1, where a and b are
 175 magnification factors used to control the network width. The specific contents of each part are as follows.

176 Table 1. The details of CloudRVE training architecture.

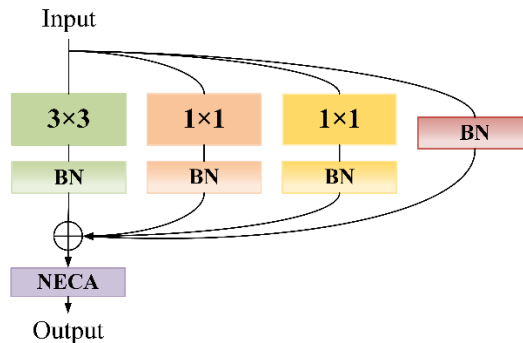
Stage	Blocks of each stage	Output size	Output channels
1	1	224×224	Min (64, 64a)
2	2	112×112	64a
3	4	56×56	128a
4	14	28×28	256a
5	1	14×14	512b

177 2.2 Broadening the CloudRVE Block of Residual Structure

178 Before the machine learning technology became mature, the classification of ground-based cloud images used hand-
 179 made features or shallow learning strategies, which took a long time and had poor accuracy (Xiao et al., 2016). With
 180 the continuous development of deep learning, CNN has been gradually applied to the task of ground-based cloud
 181 image classification and has become the mainstream method. CNN is a deep learning model including convolution
 182 calculation, including feedforward neural network, which has representation learning ability, similar to artificial
 183 neural network multilayer perceptron (Shi et al., 2017). In 2014, the most representative convolution neural network
 184 VGG came out, which adopted a single-branch topology structure, greatly improved the image processing effect and
 185 model inference speed, and became a new direction for scholars to learn and develop. With the in-depth study of the
 186 VGG, its potential in image processing is close to saturation. Scholars realize that the VGG has some shortcomings
 187 such as simple network structure, few network layers, and large parameters, which makes it difficult to extract high-
 188 order features of images and has limited image-processing performance. Therefore, improving network complexity
 189 and increasing the number of network layers has become a new research direction. The ResNet developed by (He et
 190 al., 2016) differed from the traditional neural network stacked by convolution layer and pooling layer. The network
 191 was stacked by residual modules, which not only increased the complexity of the network structure and reduced the
 192 number of network parameters, but also perfectly solved the problem of gradient disappearance or gradient explosion
 193 caused by increasing the number of network layers, which could extract abstract image features with semantic
 194 information and effectively improve image-processing performance. By improving the complexity and depth of the
 195 network, the ResNet could train the CNN model with higher accuracy, but there were numerous redundancies in its

196 residual network, impeding the network inference speed and reducing the accuracy of image processing results
 197 (Szegedy et al., 2015). Therefore, increasing the complexity and depth of the network, weakening its influence on
 198 inference speed, and improving the classification effect of ground-based cloud images become the key goals of this
 199 study.

200 To improve the classification effect of the ground-based cloud images, the CloudRVE training process is composed
 201 of CloudRVE blocks that adopt the multi-branch topology. The CloudRVE Block contains four branches and the
 202 improved channel attention module NECA. Its main branch contains a convolutional layer with a convolution kernel
 203 size of 3×3 , which can inspect the input images with a larger neighborhood scope and extract global features easily.
 204 Ground-based cloud images contain abundant cloud shape and cloud amount information, while a large convolution
 205 kernel tends to ignore cloud boundary features, resulting in inadequate feature extraction from ground-based cloud
 206 images. Therefore, the two bypass branches of CloudRVE Block adopt the convolution layer with the convolution
 207 kernel size of 1×1 , which can not only extract fine cloud boundary features and abstract cloud cover features but also
 208 keep the output dimension consistent with the input dimension, facilitating the multi-branch ground-based cloud
 209 image feature fusion. The third bypass branch of CloudRVE Block adopts the Identity branch, whose purpose is to
 210 take the input as the output and change the learning objective to the residual result approaching 0 so that the accuracy
 211 does not decline with the deepening of the network. In addition, each branch is connected to the BN layer, not only to
 212 avoid overfitting but also to prevent gradient disappearance or explosion. The specific structure of CloudRVE Block
 213 is shown in Figure 4. The input feature maps pass through three branches with a convolutional layer and BN layer at
 214 the same time. The output obtained by the input feature maps is summed with the Identity branch and input into the
 215 NECA module to obtain the final output feature.



216

217 **Figure 4: CloudRVE Block structure.**

218 2.3 NECA Module Focusing on Full Image Features

219 The attention mechanism is to let the neural network have the information processing way to distinguish the key points
 220 and to capture the connection between global information and local information flexibly. Its purpose is to enable the
 221 model to obtain the target region that needs to be focused on, put more weight on this part, highlight significant useful

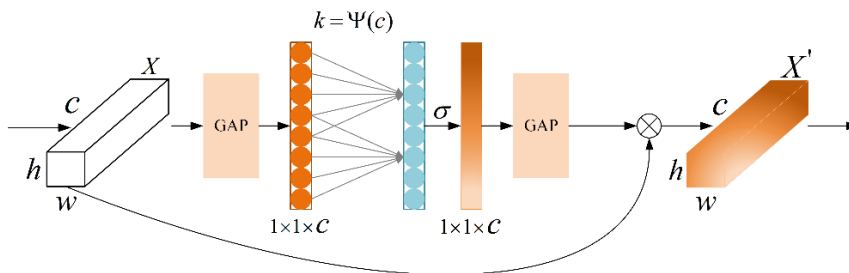
222 features, and suppress and ignore irrelevant features. The NECA (New Efficient Channel Attention) is an
 223 implementation form of channel attention mechanism, which can strengthen channel features without changing the
 224 size of the input feature maps. It adopts a local cross-channel interaction strategy without dimensionality reduction so
 225 that the 1×1 convolution layer can replace the full connection layer to learn channel attention information, which can
 226 effectively avoid the negative impact of dimensionality reduction on channel attention learning. The network
 227 performance is guaranteed and the complexity of the model is significantly reduced.

228 The ground-based cloud image samples in Figure 2 were taken by the all-sky imager and could cover the sky in
 229 this area. However, the ground-based cloud images contain not only the valid area of the whole sky but also the black
 230 invalid area. Therefore, the NECA module abandons the traditional global maximum pooling and adopts double global
 231 average pooling. The global average pooling formulas are as follows:

$$232 \gamma_{gap} = \frac{1}{wh} \sum_{i=1, j=1}^{w, h} X_{ij}, X \in R^{w \times h \times c}, \quad (1)$$

$$233 \eta_{gap} = \sigma(V_k^{gap} \gamma_{gap}), V_k^{gap} \in R^{c \times c}, \quad (2)$$

234 where X and X' represent the input and output feature maps, respectively, whereas w , h , and c are the width, height,
 235 and number of channels of the input feature map. The NECA module adopts a double global average pool, which can
 236 effectively improve its noise suppression ability and enhance its channel feature extraction ability, which can avoid
 237 the black invalid part of the feature calculation. The NECA module structure is shown in Figure 5.



238

N

239 **Figure 5: NECA model structure.**

240 Here b and r are fixed values, and their values are set to 1 and 2, respectively, while k represents the convolution
 241 kernel size and has a corresponding relationship with c . As the network deepens, the number of channels c increases
 242 by the power of 2. Therefore, k should not be a fixed value, but a dynamic change and its relationship are as follows:

$$243 C = \phi(k) = 2^{(\gamma * k - b)} \quad (3)$$

$$244 K = \psi(C) = \left\lfloor \frac{\log_2(c)}{r} - \frac{b}{r} \right\rfloor_{\text{odd}} \quad (4)$$

2.4 Inference Process from Multi-Branch to Single-Branch

The residual module is crucial to the CloudRVE training process. Its multi-branch topology can improve CloudRVE Block's ability to extract ground cloud image features and solve optimization problems such as gradient disappearance and gradient explosion caused by increasing network depth. However, the multi-branch topology will occupy more memory for the CloudRVE reasoning process, resulting in insufficient utilization of hardware computing power and slower reasoning speed. If the single-branch topology is adopted, the computing load is reduced and the inference time is saved, thus reducing memory consumption. Therefore, the single-branch topology structure is adopted in the CloudRVE inference stage, and the trained CloudRVE Block needs to be transformed into a single-branch topology model through structural re-parameterization. The conversion process mainly includes the fusion of the convolutional layer and BN layer, the conversion of the BN layer into a convolutional layer, and the fusion of the multi-branch convolutional layer. We use $W_{(3)} \in R^{C_1 \times C_2 \times 3 \times 3}$ as 3×3 convolution layers, and use C_1, C_2 as input channels and output channels respectively, and use $W_{(1)} \in R^{C_1 \times C_2 \times 1 \times 1}$ as 1×1 convolution layers. In addition, we use $\mu_{(3)}, \sigma_{(3)}, \gamma_{(3)}, \beta_{(3)}$ to represent the mean value, standard deviation, learning scaling factor, and deviation of the BN layer of the main branch, and use $\mu_{(1)}, \sigma_{(1)}, \gamma_{(1)}, \beta_{(1)}$ to represent the parameters of the BN layer of the by-pass branch containing 1×1 convolution layer, and use $\mu_{(0)}, \sigma_{(0)}, \gamma_{(0)}, \beta_{(0)}$ to represent the parameters of the BN layer of the identity branch, and use $M_{(1)} \in R^{N \times C_1 \times H_1 \times W_1}, M_{(2)} \in R^{N \times C_2 \times H_2 \times W_2}$ to represent the input and output. The CloudRVE Block structure reparameterization calculation process is as follows:

$$M_{(2)} = \text{BN}(M_{(1)} * W_{(3)}, \mu_{(3)}, \sigma_{(3)}, \gamma_{(3)}, \beta_{(3)}) + \text{BN}(M_{(1)} * W_{(1)}, \mu_{(1)}, \sigma_{(1)}, \gamma_{(1)}, \beta_{(1)}) + \text{BN}(M_{(1)}, \mu_{(0)}, \sigma_{(0)}, \gamma_{(0)}, \beta_{(0)}) \quad (5)$$

The input feature map is inputted into the NECA module through the 3×3 convolution layer completed by fusion. The process is shown in Figure 6.

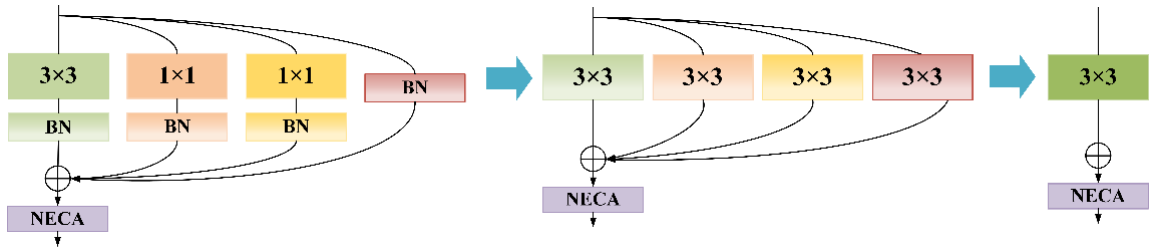


Figure 6: Re-parameterization process of CloudRVE Block structure.

2.4.1 Fusion of Convolutional Layer and BN Layer

This section first describes the fusion of the main branch 3×3 convolution layer with the BN layer and then describes the transformation of the bypass branch 1×1 convolution layer into the 3×3 convolution layer and fusion with the BN layer. In the inference stage, the number of convolutional kernel channels in the convolution layer is the same as the

271 number of channels in the input feature map, and the number of convolutional kernel channels in the output feature
 272 map is the same. The main parameters of the BN layer include mean μ , variance σ^2 , learning ratio factor γ , and
 273 deviation β . Of these, μ and σ^2 are obtained statistically in the training stage, while γ and β are obtained by learning
 274 in the training stage. The calculation of the i channel of the input BN layer is performed as follows:

$$275 \quad y_i = \frac{x_i - \mu_i}{\sqrt{\sigma_i^2 + \varepsilon}} \times \gamma_i + \beta_i, \quad (6)$$

276 where x is the input and ε is the constant approaching 0. The calculation process of the i channel input BN in the
 277 feature map can be expressed as follows:

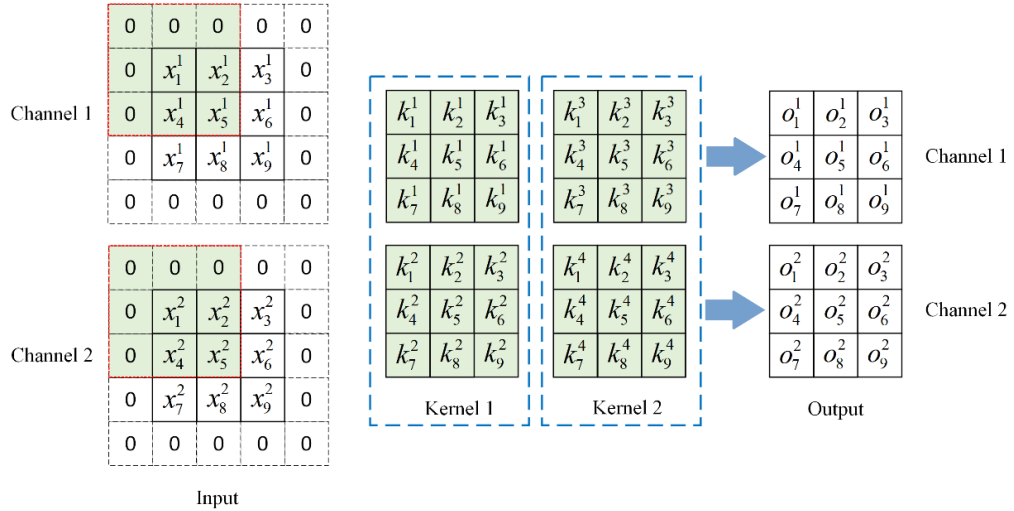
$$278 \quad bn(M, \mu, \sigma, \gamma, \beta)_{:,i,:} = (M_{:,i,:} - \mu_i) \frac{\gamma_i}{\sigma_i} + \beta_i = \frac{\gamma_i}{\sigma_i} M_{:,i,:} + \beta_i - \frac{\gamma_i}{\sigma_i} \mu_i, \quad (7)$$

279 where M is the output feature map obtained by weighted summation of the convolution layer, input to BN layer and
 280 ignore x . Therefore, we can multiply γ_i/σ_i to the i convolution kernel of the 3×3 convolution layer:

$$281 \quad W'_{i,:} = \frac{\gamma_i}{\sigma_i} W_{i,:} \quad (8)$$

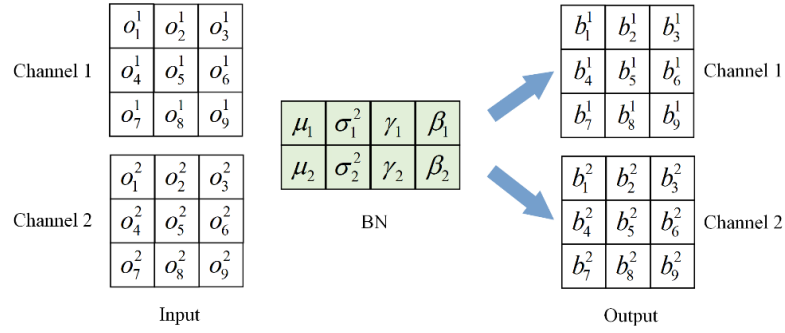
$$282 \quad b'_i = \beta_i - \frac{\mu_i \gamma_i}{\sigma_i} \quad (9)$$

283 The i convolution kernel weight of the fusion of the 3×3 convolution layer and BN layer is obtained, and the
 284 specific fusion process is shown in Figures 7 and 8. The input channel C_1 and output channel C_2 make two, and the
 285 stride is one. In the convolution layer, the input feature map is calculated by convolution to obtain the output feature
 286 map with the number of channels 2. Figure 8 shows that the number of channels in the BN layer is 2, and the output
 287 feature map of the convolution layer is used as the input feature map of the BN layer. The output feature map with
 288 the number of channels being 2 is obtained via equation (2).



289

290 **Figure 7: Input feature map through convolution layer process. For visualization, we assume that $C_1=C_2=2$.**



291

292 **Figure 8: Convolutional layer output feature map through the BN layer process.**

293 In addition, to ensure that the size of the output feature map is consistent with that of the input feature map, the input
294 feature map should be converted into 5×5 size by padding operation. The concrete convolution is as follows:

$$295 \quad o_1^1 = x_1^1 \cdot k_5^1 + x_2^1 \cdot k_6^1 + x_4^1 \cdot k_8^1 + x_5^1 \cdot k_9^1 + x_1^2 \cdot k_5^2 + x_2^2 \cdot k_6^2 + x_4^2 \cdot k_8^2 + x_5^2 \cdot k_9^2 \quad (10)$$

296 The specific calculation process of the input feature map through the BN layer is

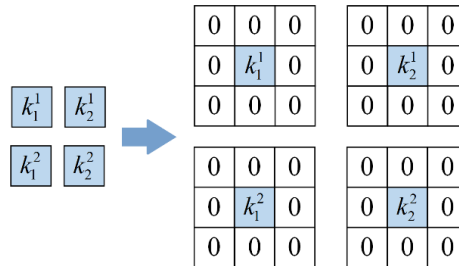
$$297 \quad b_1 = \frac{(x_1^1 \cdot k_5^1 + x_2^1 \cdot k_6^1 + x_4^1 \cdot k_8^1 + x_5^1 \cdot k_9^1 + x_1^2 \cdot k_5^2 + x_2^2 \cdot k_6^2 + x_4^2 \cdot k_8^2 + x_5^2 \cdot k_9^2) - \mu_1}{\sqrt{\sigma^2 + \varepsilon}} \cdot \gamma_1 + \beta_1 \quad (11)$$

298 Re-arranging equation (7) yields

$$299 \quad b_1 = (x_1^1 \cdot k_5^1 + x_2^1 \cdot k_6^1 + x_4^1 \cdot k_8^1 + x_5^1 \cdot k_9^1 + x_1^2 \cdot k_5^2 + x_2^2 \cdot k_6^2 + x_4^2 \cdot k_8^2 + x_5^2 \cdot k_9^2) \cdot \frac{\gamma_1}{\sqrt{\sigma^2 + \varepsilon}} + \left(\beta_1 - \frac{\mu_1}{\sqrt{\sigma^2 + \varepsilon}} \right) \quad (12)$$

$$300 \quad c = \frac{\gamma_1}{\sqrt{\sigma^2 + \varepsilon}} ; \quad d = \beta_1 - \frac{\mu_1}{\sqrt{\sigma^2 + \varepsilon}} \quad (13)$$

301 In equation (8), c and d are constants and are multiplied to the first convolution kernel of the convolution layer to
302 obtain the parameters of the first convolution kernel after the convolution layer and BN layer are fused. Other fused
303 convolution kernel parameters are calculated similarly. The convolution layer and BN layer are fused by the bypass
304 branch containing a 1×1 convolution layer. The convolution layer is first converted to 3×3 size by padding operation
305 and then fused with the BN layer by repeating the above steps. The convolution layer padding process is shown in
306 Figure 9.



307

308 **Figure 9: 1×1 convolution layer transformed into 3×3 convolution layer.**

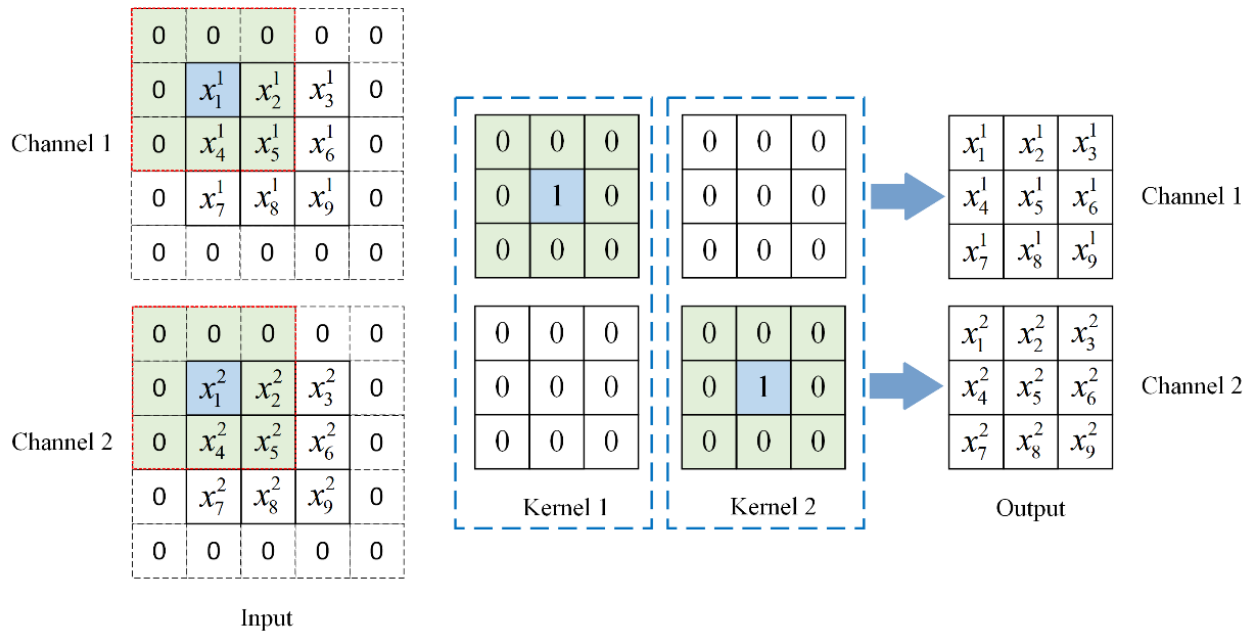
309 2.4.2 Converting the BN Layer to the Convolution Layer

310 The identity bypass branch has only a BN layer, its function is to ensure the identity mapping of the input feature map
 311 and output feature map. To realize the identical mapping between the input feature map and the output feature map in
 312 the fusion process, a 3×3 convolution layer with 2 convolution kernels and 2 convolution kernel channels needs to
 313 be designed. Secondly, the input feature map needs to be converted into a 5×5 feature map by padding operation.
 314 The specific process is shown in Figure 10. The output feature map is obtained by convolution calculation of the input
 315 feature map, and its parameters and sizes are consistent with those of the input feature map. Finally, the fusion process
 316 of the 3×3 convolution layer and BN layer is repeated to obtain a new 3×3 convolution layer.

317 2.4.3 Multi-Branch Convolution Layer Fusion

318 The structure re-parameterization transforms each branch into a 3×3 convolution layer by construction and fusion,
 319 which facilitates the fusion of multi-branch convolution layers into a single-branch 3×3 convolution. We use I and
 320 O to represent the input and output, respectively, while K_i and B_i are the convolution kernel weight and bias of the i
 321 branch. The multi-branch fusion calculation process is as follows:

$$322 \quad O = (I \otimes K_1 + B_1) + (I \otimes K_2 + B_2) + (I \otimes K_3 + B_3) + I \otimes (K_1 + K_2 + K_3) + (B_1 + B_2 + B_3) \quad (14)$$



323

324 **Figure 10: Identity branch Identity mapping process.**

325 **2.5 Warm-Up Method**

326 In this paper, the warm-up method (He et al., 2019) is used to optimize the learning rate in the model training process,
327 so that the learning rate varies in different training stages. In the initial stage of model training, a small learning rate
328 is selected, which is due to the random initialization of model weights and no prior knowledge of ground-based cloud
329 image data, and the model will quickly adjust parameters according to the input. If a large learning rate is adopted at
330 this time, the model will be overfitted and the prediction accuracy of the model will be affected. After training the
331 model for some time, the learning rate linearly increases to a preset large value and the model has some prior
332 knowledge, which can avoid overfitting and accelerate the convergence speed of the model. Finally, the model
333 distribution is relatively stable, so it is difficult to learn new features from ground-based cloud image data, and the
334 learning rate linearly approaches to zero, keeping the model stable and easily obtaining local optima.

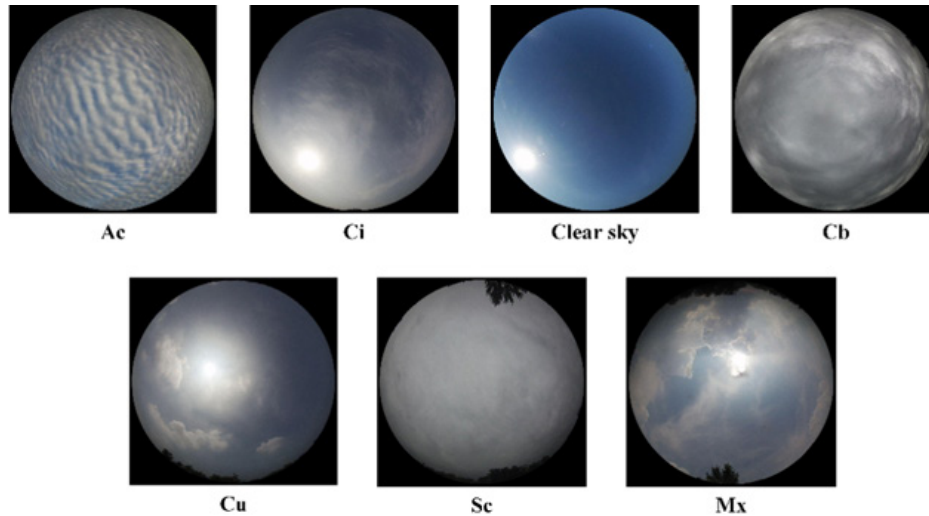
335 **3. Dataset and Experimental Settings**

336 This section introduces two kinds of ground-based cloud image classification datasets, MGCD and GRSCD, and
337 describes the relevant experimental Settings. Subsection 3.1 describes MGCD and GRSCD in detail, and Subsection
338 3.2 details experimental setting parameters and model evaluation indices.

339 **3.1 Ground-Based Cloud Image Dataset**

340 **3.1.1 Introduction to MGCD Dataset**

341 Multi-modal Ground-based Cloud image Dataset (MGCD) is the first ground-based cloud image classification dataset
342 composed of ground-based cloud images and multi-modal information, which was collected by the School of
343 Electronics and Communication Engineering of Tianjin Normal University and the Meteorological Observation
344 Center of Beijing Meteorological Bureau of China from 2017 to 2018. There are 8000 ground-based cloud images in
345 MGCD, and 4000 ground-based cloud images in the training set and testing set, including altocumulus (Ac), cirrus
346 (Ci), clear sky (Cs), cumulonimbus (Cb), cumulus (Cu), stratocumulus (Sc), and mix (Mx). In addition, cloud images
347 with a cloud cover of less than 10% are classified as clear sky, and each ground-based cloud image sample contains
348 ground-based cloud images taken at the same time and captured multimodal information. Among them, the ground-
349 based cloud images are collected by an all-sky camera with a fisheye lens, and its data storage format is JPEG with a
350 resolution of 1024×1024 pixels; Multimodal information is collected by weather stations, including temperature,
351 humidity, pressure, and wind speed, and these four elements are stored in the same vector. Figure 11 is a partial sample
352 diagram of the MGCD dataset, and the specific information is shown in Table 2.



353

354 **Figure 11: Sample legend of MGCD dataset (Liu et al., 2020a).**

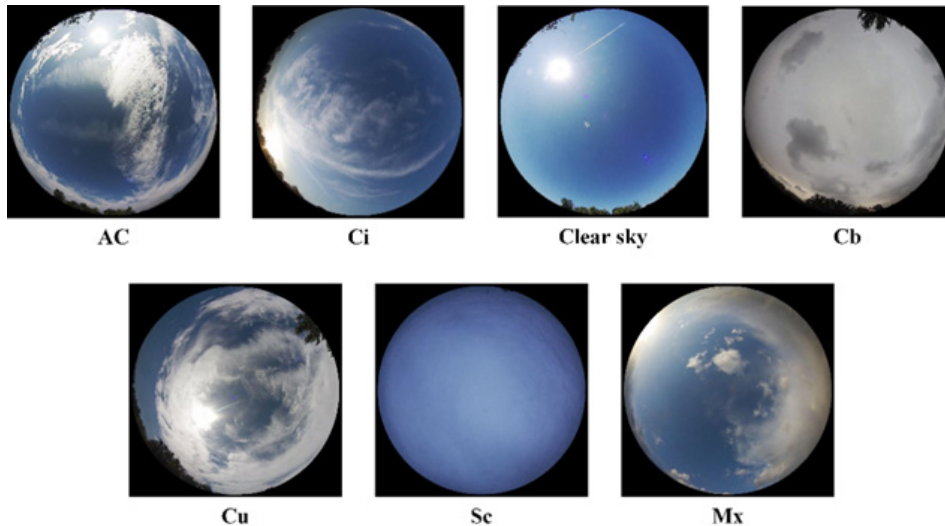
355

Table 2. MGCD dataset-specific information.

No	Class	Training	Testing	Total
1	Ac	365	366	731
2	Ci	662	661	1323
3	Cs	669	669	1338
4	Cb	593	594	1187
5	Cu	719	719	1438
6	Sc	482	481	963
7	Mx	510	510	1020
	Total	4000	4000	8000

356 3.1.2 Introduction to GRSCD Dataset

357 Ground remote sensing cloud dataset (GRSCD) is a ground-based cloud image classification dataset composed of
 358 ground-based cloud images and multimodal information. It was collected by the College of Electronic and
 359 Communication Engineering of Tianjin Normal University and the Meteorological Observation Center of Beijing
 360 Meteorological Administration of China from 2017 to 2018. There are 8000 ground-based cloud images in GRSCD,
 361 4000 ground-based cloud images in the training set, and 4000 ground-based cloud images in the testing set. There are
 362 seven types of clouds, including altocumulus (Ac), cirrus (Ci), clear sky (Cs), cumulonimbus (Cb), cumulus (Cu),
 363 stratocumulus (Sc), and mix (Mx). In addition, cloud images with less than 10% cloud cover are classified as clear
 364 skies. Each ground-based cloud image sample contains ground-based cloud images taken at the same time and
 365 captured multimodal information. Among them, the ground-based cloud images are acquired by the whole sky camera
 366 with a fish-eye lens, and its data storage format is JPEG with a resolution of 1024×1024 pixels. Multi-modal
 367 information, including temperature, humidity, pressure, and wind speed, is collected by weather stations and stored
 368 in the same vector. Figure 12 depicts a partial sample of the GRSCD dataset. The specific data are listed in Table 3.



369

370 **Figure 12: Sample legend of GRSCD dataset (Liu et al., 2020b).**

371

Table 3. GRSCD dataset-specific information

No	Class	Training	Testing	Total
1	Ac	400	331	731
2	Ci	650	673	1323
3	Cs	650	688	1338
4	Cb	600	587	1187
5	Cu	690	748	1438
6	Sc	500	463	963
7	Mx	510	510	1020
	Total	4000	4000	8000

372 3.2 Experimental Setting

373 3.2.1 Implementation Details

374 All experiments in this paper adopt Python programming language and run on Intel(R) Core (TM) i9-12700K CPU
375 @ 3.60GHz. NVIDIA GeForce RTX 3090 24G Graphical Processing Unit (GPU) platform and uses Pytorch as a deep
376 learning framework. The CNN experiment is trained on the ground-based cloud image classification datasets MGCD
377 and GRSCD respectively. The number of training data accounts for 50%, the initial learning rate is set to 0.0002,
378 Batchsize is set to 32, and Adam optimizer (Kingma and Ba, 2015) is used to optimize all available parameters in the
379 network. In addition, to improve the generalization ability of the CNN model and the convergence speed of the
380 experiment, the transfer learning method is adopted in the training stage, and model parameters are obtained by
381 training RepVGG with the ground-based cloud image classification dataset made by the team and used as the weight
382 of pre-training. CNN experiment directly trains based on pre-training weight, which can accelerate the model

383 convergence speed and shorten the training time, avoid the problem of parameter overfitting, and promote the rapid
384 gradient decline.

385 3.2.2 Evaluation Index

386 To objectively evaluate the ground-based cloud image classification performance of CloudRVE and other CNN
387 models, the accuracy rate, accuracy rate, recall rate, and the average values of different indices of 7 types of clouds in
388 MGCD and GRSCD datasets are calculated in the experiment, which is used as evaluation indices of CNN model.
389 The average accuracy rate is derived based on positive and negative samples, and the calculation process is as follows:

$$390 \text{ Accuracy}(Acc) = \frac{1}{n} \sum_{i=1}^n \frac{TP+TN}{TP+TN+FP+FN} \quad (15)$$

391 True Positive (TP) parameter indicates the sample that is correctly classified as the cloud genus, True Negative
392 (TN) indicates the sample that is correctly classified as another cloud genus, and False Positive (FN) indicates the
393 sample that is incorrectly classified as the cloud genus. False Positive (FP) parameter indicates the number of
394 misclassified samples of other cloud genera. The average accuracy rate and average recall rate can be expressed as:

$$395 \text{ Precision}(Pr) = \frac{1}{n} \sum_{i=1}^n \frac{TP}{TP+FP} \quad (16)$$

$$396 \text{ Recall}(Re) = \frac{1}{n} \sum_{i=1}^n \frac{TP}{TP+FN} \quad (17)$$

397 In addition, the average specificity and average F1_score are also used as evaluation indices of the CNN model in
398 the experiment, and their expressions are shown as follows:

$$399 \text{ Specificity}(TNR) = \frac{1}{n} \sum_{i=1}^n \frac{TN}{FP+TN} \quad (18)$$

$$400 \text{ F1_score}(F1) = \frac{1}{n} \sum_{i=1}^n \frac{2 \times Pr \times Re}{Pr + Re} \quad (19)$$

401 4. Experimental Results and Discussion

402 4.1 Classification Results of Ground-Based Cloud Images

403 The overall classification accuracy of the CloudRVE method proposed in this paper in MGCD and GRSCD datasets
404 and the classification results of each cloud genus are listed in Tables 4 and 5. It can be seen that the accuracy of
405 CloudRVE in MGCD and GRSCD datasets reached 98.15 and 98.07%, respectively. The characteristics of the Cs in
406 MGCD and GRSCD datasets were easy to identify, resulting in the accuracy rate, recall rate, specificity, and F1 value
407 reaching 100%. In the MGCD dataset, the accuracy rate, recall rate, and F1 value of the other six cloud genera all
408 exceeded 95.00%, and the specificity was above 99.50%. The accuracy and specificity of the Ci were the highest,
409 reaching 98.64 and 99.73%, respectively. Cu had the highest recall rate and F1 value, reaching 99.17 and 98.89%,

410 respectively. In addition, the recall rate and F1 value of Sc and Mx were about 2.00% lower than other cloud genera,
 411 mainly their characteristics in the MGCD dataset were similar to those of Cb and Ci, respectively, reducing
 412 CloudRVE’s ability to classify them.

413 **Table 4.** Classification results for the MGCD dataset.

Genus	Acc (%)	Pr (%)	Re (%)	TNR (%)	F1 (%)
Cu		98.62	99.17	99.70	98.89
Ac		97.02	98.08	99.70	97.55
Ci		98.64	98.94	99.73	98.79
Cs	98.15	100.0	100.0	100.0	100.0
Sc		97.26	95.84	99.63	96.54
Cb		97.13	97.13	99.51	97.13
Mx		97.24	96.67	99.60	96.95

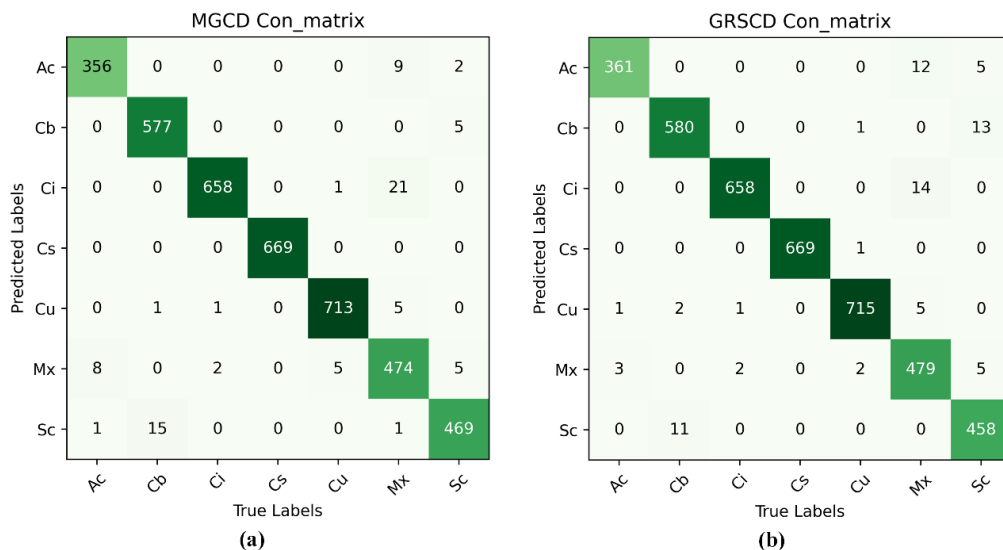
414 **Table 5.** Classification results for the GRSCD dataset.

Genus	Acc (%)	Pr (%)	Re (%)	TNR (%)	F1 (%)
Cu		99.30	99.03	99.85	99.16
Ac		94.24	98.63	99.39	96.39
Ci		97.91	99.24	99.58	98.57
Cs	98.07	100.0	100.0	100.0	100.0
Sc		98.10	96.47	99.74	97.27
Cb		97.33	98.48	99.53	97.90
Mx		97.74	93.33	99.68	95.49

415 In the GRSCD dataset, the accuracy rate, recall rate, and F1 value of the other six cloud genera exceeded 94.00%,
 416 and the specificity as over 99.30%. Cu had the highest accuracy, specificity, and F1 value, reaching 99.30, 99.85, and
 417 99.16%. The recall rate of Ci was the highest, reaching 99.17%. In addition, the Ac accuracy was only 94.24%, mainly
 418 because Ac contained a small amount of Sc, and CloudRVE could easily to misjudge Ac as Sc or Mx. Mx contained
 419 a variety of other clouds, and the images composition was complex. Cloud clusters of different can genera varied in
 420 size and shape, resulting in lower recall rate and F1 values.

421 Figure 13 shows the confusion matrix of MGCD and GRSCD datasets, showing CloudRVE prediction results on
 422 MGCD and GRSCD datasets. The horizontal axis represents the true cloud image classification, while the vertical
 423 axis represents the predicted cloud image classification, where the value of the diagonal element represents the correct
 424 number of cloud image classifications and the value of the off-diagonal element represents the number of cloud image
 425 classification errors. As can be seen from Figure 13(a), in the MGCD dataset, the correct classification of the Cu is
 426 the largest, while the misclassification of the cloud images mainly comes from Sc and Mx. The reason is that the cloud
 427 base of Sc is blackened by illumination, making it easily confused with Cb. In addition, the dynamic change of cloud

428 will lead to a change in the viewpoint of the whole sky camera, thus increasing the difficulty of cloud genus
 429 identification. As can be seen in Figure 13(b), in the GRSCD dataset, the correctly classified cloud images of the same
 430 Cu had the largest number, while the incorrectly classified ones mainly came from Mx and Sc. The Mx cloud is a
 431 hybrid cloud, containing a variety of different cloud genera, with large shares of Ac, Ci, and Cu, which could be
 432 erroneously classified as Mx. Similarly, Sc could be taken for Cb, due to their similar features, impeding the correct
 433 identification.



434

435 **Figure 13: Confusion matrix images. (a)MGCD confusion matrix image. (b) GRSCD confusion matrix image.**

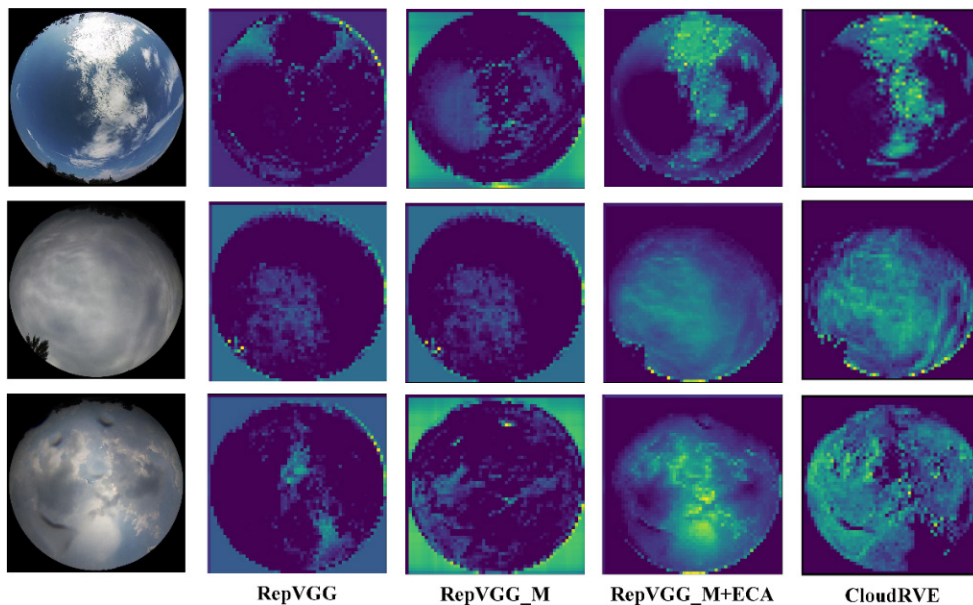
436 4.2. Ablation Experiment

437 In this section, the ablation experiment is used to compare the original structure and different improvement stages of
 438 the proposed method on the MGCD and GRSCD datasets respectively, and the results are shown in Table 6.
 439 RepVGG_M is the main improved network, ECA is the attention module, CloudRVE is the combined improved
 440 network of RepVGG_M and NECA, and is the final version of the method proposed in this paper. It can be seen from
 441 the data in the table that the performance of each improvement stage of the network model is improved compared to
 442 the previous stage, which not only verifies the feasibility of extracting more cloud image detail features by adding
 443 1×1 convolutional layer branches but also verifies that NECA can effectively improve the noise suppression ability
 444 and enhance the channel feature extraction ability. Compared with the original network structure, the accuracy of
 445 CloudRVE in the MGCD dataset increased by 2.58%, the average accuracy rate increased by 2.68%, the average
 446 recall rate increased by 2.99%, the average specificity increased by 0.42%, and the average F1 value increased by
 447 2.69%. In the GRSCD dataset, the accuracy rate increased by 2.65%, the average accuracy rate increased by 2.81%,
 448 the average specificity increased by 0.44%, and the average F1 value increased by 2.69%. Therefore, it can be seen
 449 from the data display that the method proposed in this paper has the best performance.

Table 6. Results of the ablation experiment.

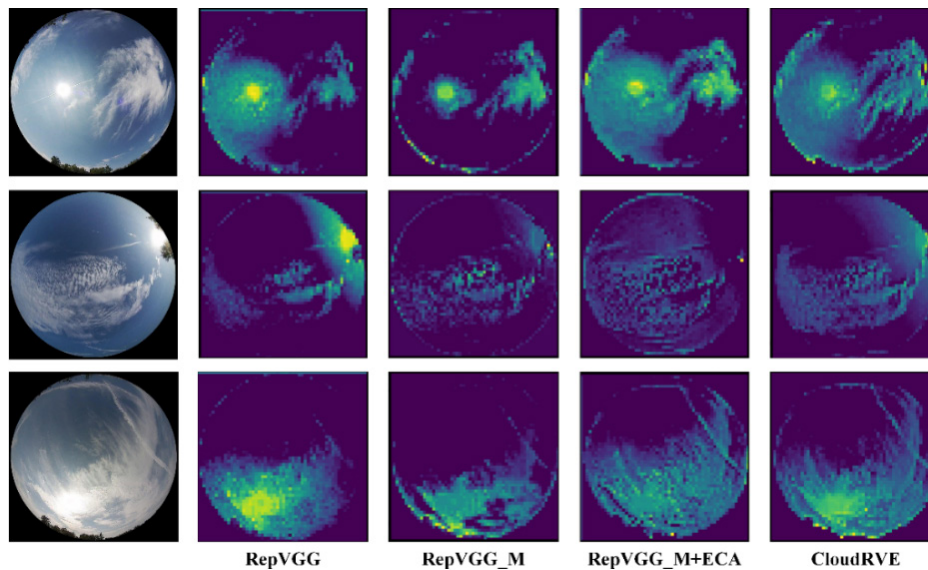
Dataset	Model	Acc (%)	Pr (%)	Re (%)	TNR (%)	F1 (%)
MGCD	RepVGG	95.57	95.31	94.99	99.26	95.14
	RepVGG_M	95.97	95.65	95.67	99.33	95.56
	RepVGG_M+ECA	96.80	96.60	96.37	99.47	96.45
	CloudRVE	98.15	97.99	97.98	99.68	97.83
GRSCD	RepVGG	95.42	94.99	94.88	99.24	94.92
	RepVGG_M	95.70	95.46	95.30	99.29	95.36
	RepVGG_M+ECA	96.10	95.67	95.74	99.35	95.68
	CloudRVE	98.07	97.80	97.88	99.68	97.82

451 To visually compare the performance of the original structure and the method proposed in this paper in different
452 improvement stages, we visualize the features by extracting the feature map of the middle layer of the network and
453 then explain the feature extraction ability of the original structure and the method proposed in this paper in different
454 improvement stages, as shown in Figures 14 and 15. The method generates a rough feature map to display the
455 important region of the predicted images through the parameter weights generated by network training, in which the
456 brighter the region indicates the higher its importance, and the darker the region represents the sky or those that cannot
457 be extracted. Figure 14 shows that CloudRVE has the best feature location and extraction ability by showing the
458 feature maps of three different cloud images in the MGCD dataset. Figure 15 shows that the three cloud images of the
459 GRSCD dataset include not only clouds and sky but also strong sunlight, which affects the classification accuracy of
460 the model. However, it can be seen from the feature maps that CloudRVE not only has the best feature extraction
461 ability but also has a strong ability to suppress noise such as sunlight.



462

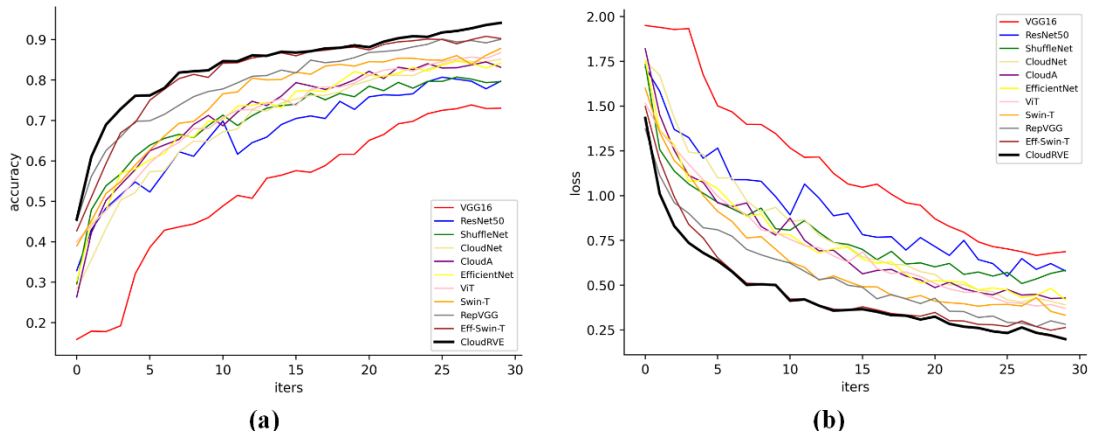
463 **Figure 14: Feature extraction of different models based on MGCD (Liu et al., 2020a).**



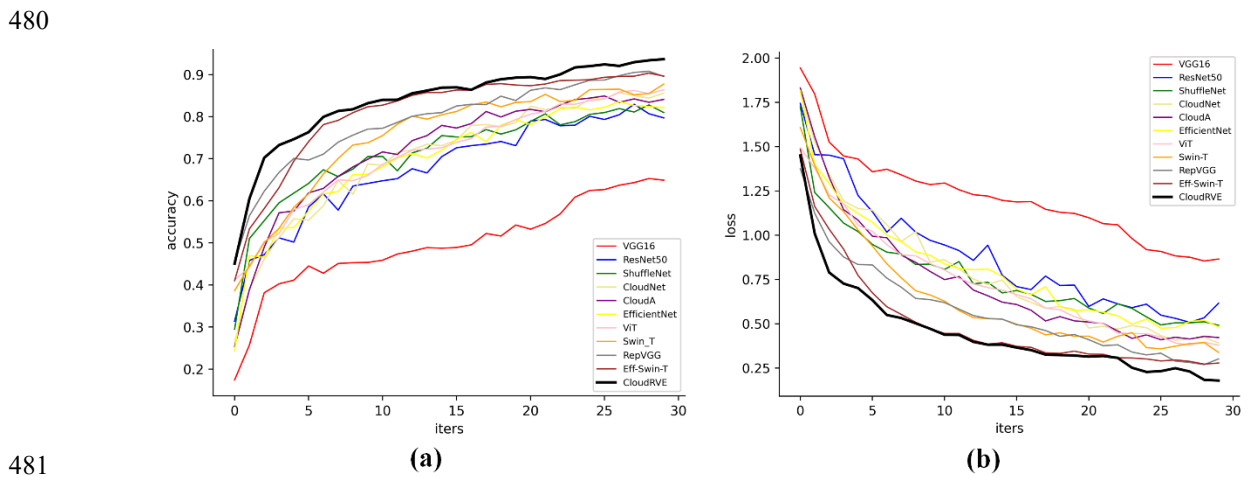
465

466 **Figure 15: Feature extraction of different models based on GRSCD (Liu et al., 2020b).**467 **4.3 Comparison of Experimental Results**

468 To verify the feasibility of the proposed CloudRVE method, we compared it with other advanced methods, including
 469 CloudNet (Zhang et al., 2018), CloudA (Wang et al., 2020), Eff-Swin-T (Li et al., 2022), and other ground-based
 470 cloud image classification methods. These included such classic CNN models as VGG16 (Szegedy et al., 2015),
 471 ResNet50 (He et al., 2016), ShuffleNet (Zhang et al., 2018) and EfficientNet (Tan and Le, 2019). In addition, we
 472 compared it with other Transformer-based classification models such as ViT-L (Dosovitskiy et al., 2022), Swin-T(Liu
 473 et al., 2021), etc. Figures 16 and 17 illustrate the performances of different methods by displaying the training accuracy
 474 and training loss curves of MGCD and GRSCD datasets. Here the black bold curve represents the CloudRVE method,
 475 which has the largest accuracy value, the fastest convergence rate, the smallest loss rate, and the fastest decline rate
 476 in the training stage. This strongly indicates that the CloudRVE method has the best classification performance of
 477 ground-based cloud images.



478 (a)
 479 Figure 16: Training accuracy (a) and training loss (b) curves of the MGCD dataset.



481 (a)
 482 Figure 17: Training accuracy (a) and training loss (b) curves of the GRSCD dataset.

483 The comparative analysis results of the above methods are summarized in Table 7. It can be seen from the
 484 experimental results that RepVGG had the best performance among the CNN-based methods. The accuracy rate,
 485 accuracy rate, recall rate, specificity, and F1 value for the MGCD dataset reached 95.57, 95.31, 94.99, 99.26, and
 486 95.14%, respectively, while those for the GRSCD dataset were 95.42, 94.99, 94.88, 99.24, and 94.92%, respectively.
 487 Ground-based cloud images have more texture features and deep semantic features than other images, and more image
 488 features need to be obtained to meet the classification requirements of such images. In recent years, Transformer has
 489 been widely used for image processing tasks due to its strong feature extraction capability. Several scholars have
 490 improved the Transformer derivative model through continuous exploration. Among them, Eff-Swin-T was an
 491 improvement based on Swin-T, and its performance on MGCD and GRSCD datasets was better than that of the classic
 492 CNN model. Its accuracy rate, accuracy rate, recall rate, specificity, and F1 value reached 96.93, 96.73, 96.44, 99.49,
 493 96.56%, and 95.62, 95.41, 95.11, 99.27, 95.21%, respectively. Compared with Transformer and classical networks,

494 the proposed method had much better classification performance of ground-based cloud images. For different cloud
 495 image classification datasets, it exhibited excellent generalization ability and strong robustness, which is instrumental
 496 in photovoltaic power generation prediction.

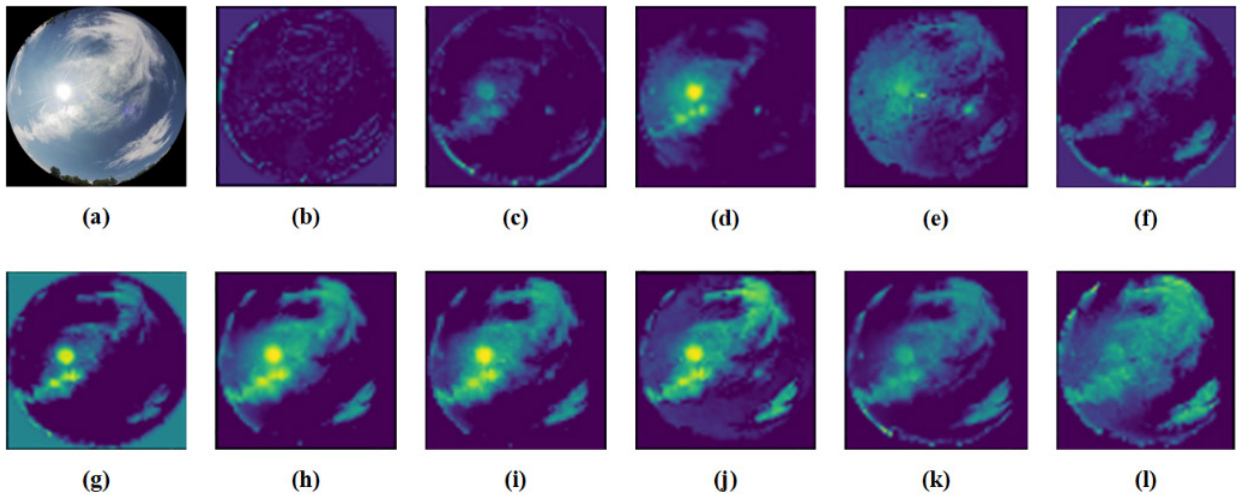
497 **Table 7.** Comparison of experimental results.

Method	MGCD					GRSCD				
	Acc (%)	Pr (%)	Re (%)	TNR (%)	F1 (%)	Acc (%)	Pr (%)	Re (%)	TNR (%)	F1 (%)
VGG-16	78.25	77.04	75.52	96.36	75.55	73.50	73.88	70.29	95.53	70.87
ResNet-50	85.98	85.24	84.55	97.67	84.82	86.51	85.56	85.38	97.75	85.34
ShuffleNet	86.95	86.08	85.68	97.83	85.71	86.99	86.85	85.18	97.82	85.71
CloudNet	90.01	89.24	89.08	98.34	89.13	89.60	89.06	88.60	98.27	88.79
CloudA	89.62	88.78	88.50	98.28	88.61	90.03	89.54	88.71	98.34	89.03
EfficientNet	91.17	90.66	90.22	98.53	90.27	90.10	89.68	88.92	98.35	89.13
ViT-L	91.11	90.91	90.21	98.55	90.40	90.98	90.49	90.33	98.50	90.39
Swin-T	92.87	92.44	91.63	98.63	91.76	93.55	93.22	92.87	98.93	92.71
RepVGG	95.57	95.31	94.99	99.26	95.14	95.42	94.99	94.88	99.24	94.92
Eff-Swin-T	96.93	96.73	96.44	99.49	96.56	95.62	95.41	95.11	99.27	95.21
CloudRVE	98.15	97.99	97.98	99.68	97.83	98.07	97.80	97.88	99.68	97.82

498 The space complexities of CloudRVE and ten alternative methods are summarized and compared in Table 8. It can
 499 be seen from the table that CloudRVE had a spatial complexity of 105.17 Mb, which is in line with the spatial
 500 complexity of Swin-T and Eff-Swin-T, and far less than the spatial complexity of ViT-L. The spatial complexity of
 501 CloudRVE exceeded that of RepVGG by three times, achieving the best ground cloud image classification
 502 performance. Thus, CloudRVE achieved excellent ground cloud image classification performance at the expense of
 503 higher spatial complexity.

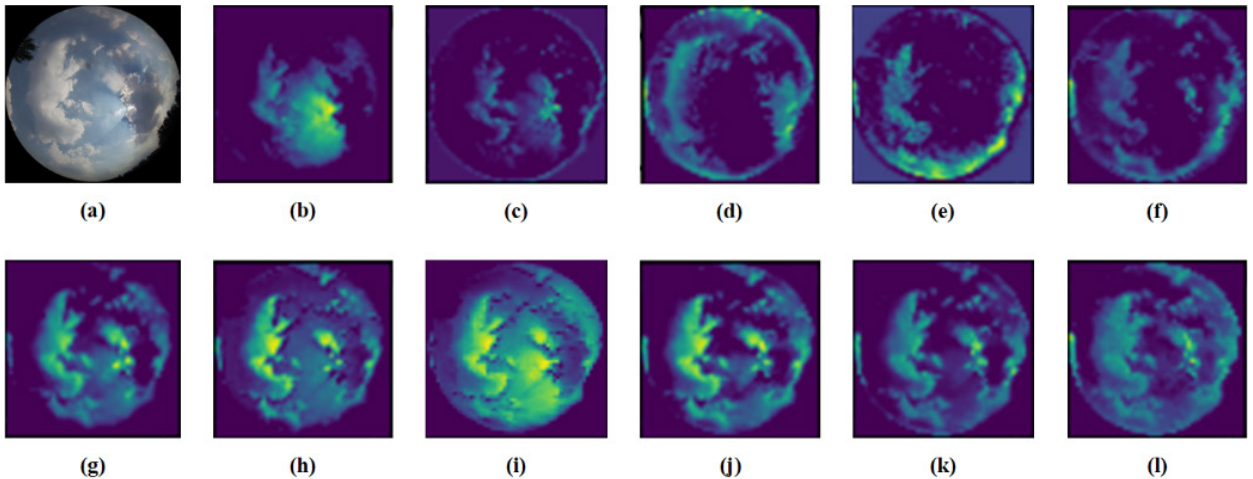
504 **Table 8.** Space complexity of the proposed and ten alternative methods.

Method	Space complexity (Mb)
VGG-16	512.28
ResNet-50	90.03
ShuffleNet	4.93
CloudNet	153.36
CloudA	87.57
EfficientNet	15.61
ViT-L	327.37
Swin-T	105.28
RepVGG	30.10
Eff-Swin-T	105.24
CloudRVE	105.17



505

506 **Figure 18: Feature extraction of different methods based on MGCD, (a) Original (Liu et al., 2020a); (b)VGG-16; (c) ResNet-**
 507 **50; (d) ShuffleNet; (e) CloudNet; (f) CloudA; (g) EfficientNet; (h) ViT-L; (i) Swin-T; (j) RepVGG; (k) Eff-Swin-T; (l)**
 508 **CloudRVE**



509

510 **Figure 19: Feature extraction of different methods based on GRSCD: (a) Original (Liu et al., 2020b); (b)VGG-16;**
 511 **(c)ResNet-50; (d) ShuffleNet; (e) CloudNet; (f) CloudA; (g) EfficientNet; (h) ViT-L; (i) Swin-T; (j) RepVGG; (k) Eff-Swin-**
 512 **T; (l) CloudRVE**

513 In order to provide a more intuitive display of the advantages of CloudRVE over other advanced methods, we
 514 extracted the features of the intermediate layers of different methods to generate the ground cloud feature maps for
 515 the building foundation, demonstrating the strong feature extraction capabilities of CloudRVE and proving its
 516 superiority, as shown in Figures 18 and 19. Feature extraction was achieved by generating rough feature maps through
 517 network training with parameter weights to highlight the important regions of predicted images. The light colored
 518 regions represent the important features, while the dark colored regions represent the sky or unsuccessfully extracted
 519 features. Figure 18(b-i) shows the feature maps of different ground cloud classification methods based on MGCD

520 dataset to demonstrate the CloudRVE capability to extract more extensive and comprehensive cloud features and
521 suppress the black regions and sunlight, further illustrating the best feature localization and extraction capability of
522 CloudRVE. Figure 19(b-i) shows the feature maps of different ground cloud classification methods based on GRSCD
523 dataset to demonstrate that the cloud feature extracted by CloudRVE covers the effective area in Figure 19(a) with
524 the best coverage and the best suppression of the sunlight, further proving that CloudRVE has the best feature
525 localization and extraction capabilities.

526 **5. Conclusion**

527 This study proposed a new classification method called CloudRVE (Cloud Representative Volume Element Network)
528 for ground-based cloud images based on the improved RepVGG network. In particular, its training stage structure
529 was improved, the residual structure was broadened, and 1×1 convolutional layer branches were added to each block,
530 extending the gradient information of the topology structure and enhancing the network ability to represent boundary
531 features of cloud images. In addition, the NECA (New Efficient Channel Attention) module was embedded after
532 multi-branch fusion to learn the feature relationship between sequences, improve the network cross-channel
533 interaction ability, and extract the best global features of cloud images. We validated the excellent performance of the
534 proposed method on MGCD and GRSCD ground-based cloud image datasets, achieving the classification accuracy
535 values of 98.15 and 98.07%, respectively, which outperformed ten other advanced methods. The particular
536 contributions of this paper were summarized in Section 1. However, this study shares some limitations with other
537 methods of classifying ground-based cloud images via convolutional neural networks, which have reached a
538 bottleneck due to continuous expansion of the capacity of ground-based cloud image datasets. A lucrative alternative
539 is Transformer, which got a high reputation of a powerful deep neural network for processing sequences but has
540 received little attention in ground-based cloud image classification. On the other hand, cloud classification is only
541 based on ground-based cloud image features, while many physical features, such as height, thickness, etc., may be
542 also used. Our follow-up study envisages combining CNN and Transformer models and using cloud height, cloud
543 thickness, and other parameters in ground-based cloud image classification to improve the model's performance.

544

545 **Author Contributions.** LH performed the experiments and wrote the paper. CS, KZ, and HX analyzed the data and
546 designed the experiments. CS conceived the method and reviewed the paper. XL, ZS, and XZ reviewed the paper and
547 gave constructive suggestions.

548 **Financial support.** This research was funded by the National Science Foundation of China (NSFC) under Grant No.
549 62076093 and No. 62206095 and through the Fundamental Research Funds for the Central Universities of China
550 under Grant No. 2022MS078 and No. 2020MS099.

551

552 **Data Availability Statement.** The MGCD dataset was accessed from <https://github.com/shuangliutjnu/Multimodal->
553 <https://github.com/shuangliutjnu/TJNU->
554 <https://github.com/shuangliutjnu/TJNU->
555 <https://github.com/shuangliutjnu/TJNU->
556 <https://github.com/shuangliutjnu/TJNU->
557 <https://github.com/shuangliutjnu/TJNU->
558 <https://github.com/shuangliutjnu/TJNU->
559 <https://github.com/shuangliutjnu/TJNU->
560 <https://github.com/shuangliutjnu/TJNU->
561 <https://github.com/shuangliutjnu/TJNU->
562 <https://github.com/shuangliutjnu/TJNU->
563 <https://github.com/shuangliutjnu/TJNU->
564 <https://github.com/shuangliutjnu/TJNU->
565 <https://github.com/shuangliutjnu/TJNU->
566 <https://github.com/shuangliutjnu/TJNU->
567 <https://github.com/shuangliutjnu/TJNU->
568 <https://github.com/shuangliutjnu/TJNU->
569 <https://github.com/shuangliutjnu/TJNU->
570 <https://github.com/shuangliutjnu/TJNU->
571 <https://github.com/shuangliutjnu/TJNU->
572 <https://github.com/shuangliutjnu/TJNU->
573 <https://github.com/shuangliutjnu/TJNU->
574 <https://github.com/shuangliutjnu/TJNU->
575 <https://github.com/shuangliutjnu/TJNU->
576 <https://github.com/shuangliutjnu/TJNU->
577 <https://github.com/shuangliutjnu/TJNU->
578 <https://github.com/shuangliutjnu/TJNU->
579 <https://github.com/shuangliutjnu/TJNU->
580 <https://github.com/shuangliutjnu/TJNU->
581 <https://github.com/shuangliutjnu/TJNU->

555

556 **Acknowledgments.** We would like to thank Professor Liu Shuang of Tianjin Normal University for providing the
557 support of ground-based cloud image classification datasets and Student Meng Ru-oxuan from Guangxi Normal
558 University for her contribution to this paper.

559

560 **Declaration of Competing Interests.** The authors declare that they have no conflict of interest.

561 **References**

562 Alonso-Montesinos, J., Martinez-Durban, M., del Sagrado, J., del Aguila, I. M., and Batlles, F. J.: The application of
563 Bayesian network classifiers to cloud classification in satellite images, *Renew. Energy*, 97, 155–161,
564 <https://doi.org/10.1016/j.renene.2016.05.066>, 2016.

565 Calbó, J. and Sabburg, J.: Feature Extraction from Whole-Sky Ground-Based Images for Cloud-Type Recognition, *J.*
566 *Atmospheric Ocean. Technol.*, 25, 3–14, <https://doi.org/10.1175/2007JTECHA959.1>, 2008.

567 Cazorla, A., Olmo, F. J., and Alados-Arboledas, L.: Development of a sky imager for cloud cover assessment, *JOSA*
568 *A*, 25, 29–39, <https://doi.org/10.1364/JOSAA.25.000029>, 2008.

569 Ding, X., Zhang, X., Ma, N., Han, J., Ding, G., and Sun, J.: RepVGG: Making VGG-style ConvNets Great Again, in:
570 2021 IEEE/CVF Conference on Computer Vision and Pattern Recognition (CVPR), 2021 IEEE/CVF Conference on
571 Computer Vision and Pattern Recognition (CVPR), 13728–13737, <https://doi.org/10.1109/CVPR46437.2021.01352>,
572 2021.

573 Dosovitskiy, A., Beyer, L., Kolesnikov, A., Weissenborn, D., Zhai, X., Unterthiner, T., Dehghani, M., Minderer, M.,
574 Heigold, G., Gelly, S., Uszkoreit, J., and Houlsby, N.: An Image is Worth 16x16 Words: Transformers for Image
575 Recognition at Scale, *International Conference on Learning Representations*, 1909, 2022.

576 Fabel, Y., Nouri, B., Wilbert, S., Blum, N., Triebel, R., Hasenbalg, M., Kuhn, P., Zarzalejo, L. F., and Pitz-Paal, R.:
577 Applying self-supervised learning for semantic cloud segmentation of all-sky images, *Atmospheric Meas. Tech.*, 15,
578 797–809, <https://doi.org/10.5194/amt-15-797-2022>, 2022.

579 Goren, T., Rosenfeld, D., Sourdeval, O., and Quaas, J.: Satellite Observations of Precipitating Marine Stratocumulus
580 Show Greater Cloud Fraction for Decoupled Clouds in Comparison to Coupled Clouds, *Geophys. Res. Lett.*, 45,
581 5126–5134, <https://doi.org/10.1029/2018GL078122>, 2018.

582 Gorodetskaya, I. V., Kneifel, S., Maahn, M., Van Tricht, K., Thiery, W., Schween, J. H., Mangold, A., Crewell, S.,
583 and Van Lipzig, N. P. M.: Cloud and precipitation properties from ground-based remote-sensing instruments in East
584 Antarctica, *The Cryosphere*, 9, 285–304, <https://doi.org/10.5194/tc-9-285-2015>, 2015.

585 Gyasi, E. K. and Swarnalatha, P.: Cloud-MobiNet: An Abridged Mobile-Net Convolutional Neural Network Model
586 for Ground-Based Cloud Classification, *Atmosphere*, 14, 280, <https://doi.org/10.3390/atmos14020280>, 2023.

587 He, K., Zhang, X., Ren, S., and Sun, J.: Deep Residual Learning for Image Recognition, in: 2016 IEEE Conference
588 on Computer Vision and Pattern Recognition (CVPR), 2016 IEEE Conference on Computer Vision and Pattern
589 Recognition (CVPR), 770–778, <https://doi.org/10.1109/CVPR.2016.90>, 2016.

590 He, T., Zhang, Z., Zhang, H., Zhang, Z., Xie, J., and Li, M.: Bag of Tricks for Image Classification with Convolutional
591 Neural Networks, 2019 IEEE/CVF Conference on Computer Vision and Pattern Recognition (CVPR), Los Alamitos,
592 558–567, <https://doi.org/10.1109/CVPR.2019.00065>, 2019.

593 Heinle, A., Macke, A., and Srivastav, A.: Automatic cloud classification of whole sky images, *Atmospheric Meas.*
594 *Tech.*, 3, 557–567, <https://doi.org/10.5194/amt-3-557-2010>, 2010.

595 Hu, J., Shen, L., and Sun, G.: Squeeze-and-Excitation Networks, in: 2018 IEEE/CVF Conference on Computer Vision
596 and Pattern Recognition, 2018 IEEE/CVF Conference on Computer Vision and Pattern Recognition, 7132–7141,
597 <https://doi.org/10.1109/CVPR.2018.00745>, 2018.

598 Ioffe, S. and Szegedy, C.: Batch Normalization: Accelerating Deep Network Training by Reducing Internal Covariate
599 Shift, in: *International Conference on Machine Learning*, Vol 37, San Diego, 448–456, 2015.

600 Johnson, R., Hering, W., and Shields, J.: Automated Visibility & Cloud Cover Measurements with a Solid State
601 Imaging System, Scripps Institution of Oceanography, Marine Physical Laboratory, University of California, San
602 Diego, 1989.

603 Kalisch, J. and Macke, A.: Estimation of the total cloud cover with high temporal resolution and parametrization of
604 short-term fluctuations of sea surface insolation, *Meteorol. Z.*, 603–611, [https://doi.org/10.1127/0941-](https://doi.org/10.1127/0941-2948/2008/0321)
605 [2948/2008/0321](https://doi.org/10.1127/0941-2948/2008/0321), 2008.

606 Kingma, D. P. and Ba, J.: Adam: A Method for Stochastic Optimization, 3rd International Conference for Learning
607 Representations, San Diego, arXiv:1412.6980 [cs], <https://doi.org/10.48550/arXiv.1412.6980>, 2015.

608 Li, X., Qiu, B., Cao, G., Wu, C., and Zhang, L.: A Novel Method for Ground-Based Cloud Image Classification Using
609 Transformer, *Remote Sens.*, 14, 3978, <https://doi.org/10.3390/rs14163978>, 2022.

610 Li, Z., Kong, H., and Wong, C.-S.: Neural Network-Based Identification of Cloud Types from Ground-Based Images
611 of Cloud Layers, *Appl. Sci.*, 13, 4470, <https://doi.org/10.3390/app13074470>, 2023.

612 Lin, F., Zhang, Y., and Wang, J.: Recent advances in intra-hour solar forecasting: A review of ground-based sky
613 image methods, *Int. J. Forecast.*, 39, 244–265, <https://doi.org/10.1016/j.ijforecast.2021.11.002>, 2023.

614 Liu, S., Li, M., Zhang, Z., Cao, X., and Durrani, T. S.: Ground-Based Cloud Classification Using Task-Based Graph
615 Convolutional Network, *Geophys. Res. Lett.*, 47, e2020GL087338, <https://doi.org/10.1029/2020GL087338>, 2020a.

616 Liu, S., Li, M., Zhang, Z., Xiao, B., and Durrani, T. S.: Multi-Evidence and Multi-Modal Fusion Network for Ground-
617 Based Cloud Recognition, *Remote Sens.*, 12, 464, <https://doi.org/10.3390/rs12030464>, 2020b.

618 Liu, S., Duan, L., Zhang, Z., Cao, X., and Durrani, T. S.: Multimodal Ground-Based Remote Sensing Cloud
619 Classification via Learning Heterogeneous Deep Features, *IEEE Trans. Geosci. Remote Sens.*, 58, 7790–7800,
620 <https://doi.org/10.1109/TGRS.2020.2984265>, 2020c.

621 Liu, S., Duan, L., Zhang, Z., Cao, X., and Durrani, T. S.: Ground-Based Remote Sensing Cloud Classification via
622 Context Graph Attention Network, *IEEE Trans. Geosci. Remote Sens.*, 60, 1–11,
623 <https://doi.org/10.1109/TGRS.2021.3063255>, 2022.

624 Liu, Z., Lin, Y., Cao, Y., Hu, H., Wei, Y., Zhang, Z., Lin, S., and Guo, B.: Swin Transformer: Hierarchical Vision
625 Transformer using Shifted Windows, in: 2021 IEEE/CVF International Conference on Computer Vision (ICCV),
626 2021 IEEE/CVF International Conference on Computer Vision (ICCV), Montreal, QC, Canada, 9992–10002,
627 <https://doi.org/10.1109/ICCV48922.2021.00986>, 2021.

628 Long, C., Li, X., Jing, Y., and Shen, H.: Bishift Networks for Thick Cloud Removal with Multitemporal Remote
629 Sensing Images, *Int. J. Intell. Syst.*, 2023, e9953198, <https://doi.org/10.1155/2023/9953198>, 2023.

630 Meng, Q., Zhao, S., Huang, Z., and Zhou, F.: MagFace: A Universal Representation for Face Recognition and Quality
631 Assessment, in: 2021 IEEE/CVF Conference on Computer Vision and Pattern Recognition (CVPR), 2021 IEEE/CVF
632 Conference on Computer Vision and Pattern Recognition (CVPR), 14220–14229,
633 <https://doi.org/10.1109/CVPR46437.2021.01400>, 2021.

634 Norris, J. R., Allen, R. J., Evan, A. T., Zelinka, M. D., O’Dell, C. W., and Klein, S. A.: Evidence for climate change
635 in the satellite cloud record, *Nature*, 536, 72–75, <https://doi.org/10.1038/nature18273>, 2016.

636 Nouri, B., Kuhn, P., Wilbert, S., Hanrieder, N., Prah, C., Zarzalejo, L., Kazantzidis, A., Blanc, P., and Pitz-Paal, R.:
637 Cloud height and tracking accuracy of three all sky imager systems for individual clouds, *Sol. Energy*, 177, 213–228,
638 <https://doi.org/10.1016/j.solener.2018.10.079>, 2019.

639 Pfister, G., McKenzie, R. L., Liley, J. B., Thomas, A., Forgan, B. W., and Long, C. N.: Cloud Coverage Based on
640 All-Sky Imaging and Its Impact on Surface Solar Irradiance, *J. Appl. Meteorol. Climatol.*, 42, 1421–1434,
641 [https://doi.org/10.1175/1520-0450\(2003\)042<1421:CCBOAI>2.0.CO;2](https://doi.org/10.1175/1520-0450(2003)042<1421:CCBOAI>2.0.CO;2), 2003.

642 Qu, Y., Xu, J., Sun, Y., and Liu, D.: A temporal distributed hybrid deep learning model for day-ahead distributed PV
643 power forecasting, *Appl. Energy*, 304, 117704, <https://doi.org/10.1016/j.apenergy.2021.117704>, 2021.

644 Sarukkai, V., Jain, A., Uzgent, B., and Ermon, S.: Cloud Removal in Satellite Images Using Spatiotemporal
645 Generative Networks, in: 2020 IEEE Winter Conference on Applications of Computer Vision (WACV), 2020 IEEE
646 Winter Conference on Applications of Computer Vision (WACV), 1785–1794,
647 <https://doi.org/10.1109/WACV45572.2020.9093564>, 2020.

648 Shi, C., Wang, C., Wang, Y., and Xiao, B.: Deep Convolutional Activations-Based Features for Ground-Based Cloud
649 Classification, *IEEE Geosci. Remote Sens. Lett.*, 14, 816–820, <https://doi.org/10.1109/LGRS.2017.2681658>, 2017.

650 Shi, C., Zhou, Y., Qiu, B., He, J., Ding, M., and Wei, S.: Diurnal and nocturnal cloud segmentation of all-sky imager
651 (ASI) images using enhancement fully convolutional networks, *Atmospheric Meas. Tech.*, 12, 4713–4724,
652 <https://doi.org/10.5194/amt-12-4713-2019>, 2019.

653 Simonyan, K. and Zisserman, A.: Very Deep Convolutional Networks for Large-Scale Image Recognition,
654 <https://doi.org/10.48550/arXiv.1409.1556>, 10 April 2015.

655 Singh, M. and Glennen, M.: Automated ground-based cloud recognition, *Pattern Anal. Appl.*, 8, 258–271,
656 <https://doi.org/10.1007/s10044-005-0007-5>, 2005.

657 Szegedy, C., Liu, W., Jia, Y., Sermanet, P., Reed, S., Anguelov, D., Erhan, D., Vanhoucke, V., and Rabinovich, A.:
658 Going deeper with convolutions, in: 2015 IEEE Conference on Computer Vision and Pattern Recognition (CVPR),
659 2015 IEEE Conference on Computer Vision and Pattern Recognition (CVPR), 1–9,
660 <https://doi.org/10.1109/CVPR.2015.7298594>, 2015.

661 Tan, M. and Le, Q. V.: EfficientNet: Rethinking Model Scaling for Convolutional Neural Networks, in: International
662 Conference on Machine Learning, Vol 97, San Diego, 2019.

663 Tang, Y., Yang, P., Zhou, Z., Pan, D., Chen, J., and Zhao, X.: Improving cloud type classification of ground-based
664 images using region covariance descriptors, *Atmospheric Meas. Tech.*, 14, 737–747, [https://doi.org/10.5194/amt-14-](https://doi.org/10.5194/amt-14-737-2021)
665 [737-2021](https://doi.org/10.5194/amt-14-737-2021), 2021.

666 Taravat, A., Del Frate, F., Cornaro, C., and Vergari, S.: Neural Networks and Support Vector Machine Algorithms
667 for Automatic Cloud Classification of Whole-Sky Ground-Based Images, *IEEE Geosci. Remote Sens. Lett.*, 12, 666–
668 670, <https://doi.org/10.1109/LGRS.2014.2356616>, 2015.

669 Wang, M., Zhou, S., Yang, Z., and Liu, Z.: CloudA: A Ground-Based Cloud Classification Method with a
670 Convolutional Neural Network, *J. Atmospheric Ocean. Technol.*, 37, 1661–1668, [https://doi.org/10.1175/JTECH-D-](https://doi.org/10.1175/JTECH-D-19-0189.1)
671 [19-0189.1](https://doi.org/10.1175/JTECH-D-19-0189.1), 2020.

672 Wang, M., Zhuang, Z., Wang, K., Zhou, S., Zhou, S., and Liu, Z.: Intelligent classification of ground-based visible
673 cloud images using a transfer convolutional neural network and fine-tuning, *Opt. Express*, 29, 41176–41190,
674 <https://doi.org/10.1364/OE.442455>, 2021.

675 Wu, X., Zhan, C., Lai, Y.-K., Cheng, M.-M., and Yang, J.: A Large-Scale Benchmark Dataset for Insect Pest
676 Recognition, in: 2019 IEEE/CVF Conference on Computer Vision and Pattern Recognition (CVPR), 2019 IEEE/CVF
677 Conference on Computer Vision and Pattern Recognition (CVPR), Conference Location: Long Beach, CA, USA,
678 8779–8788, <https://doi.org/10.1109/CVPR.2019.00899>, 2019.

679 Xiao, Y., Cao, Z., Zhuo, W., Ye, L., and Zhu, L.: mCLOUD: A Multiview Visual Feature Extraction Mechanism for
680 Ground-Based Cloud Image Categorization, *J. Atmospheric Ocean. Technol.*, 33, 789–801,
681 <https://doi.org/10.1175/JTECH-D-15-0015.1>, 2016.

682 Ye, L., Cao, Z., and Xiao, Y.: DeepCloud: Ground-Based Cloud Image Categorization Using Deep Convolutional
683 Features, *IEEE Trans. Geosci. Remote Sens.*, 55, 5729–5740, <https://doi.org/10.1109/TGRS.2017.2712809>, 2017.

684 Yu, A., Tang, M., Li, G., Hou, B., Xuan, Z., Zhu, B., and Chen, T.: A Novel Robust Classification Method for Ground-
685 Based Clouds, *Atmosphere*, 12, 999, <https://doi.org/10.3390/atmos12080999>, 2021.

686 Zhang, J., Liu, P., Zhang, F., and Song, Q.: CloudNet: Ground-Based Cloud Classification With Deep Convolutional
687 Neural Network, *Geophys. Res. Lett.*, 45, 8665–8672, <https://doi.org/10.1029/2018GL077787>, 2018a.

688 Zhang, X., Zhou, X., Lin, M., and Sun, R.: ShuffleNet: An Extremely Efficient Convolutional Neural Network for
689 Mobile Devices, in: 2018 Ieee/Cvf Conference on Computer Vision and Pattern Recognition (cvpr), New York, 6848–
690 6856, <https://doi.org/10.1109/CVPR.2018.00716>, 2018b.

691 Zhang, Y., Liu, H., and Hu, Q.: TransFuse: Fusing Transformers and CNNs for Medical Image Segmentation, in:
692 Medical Image Computing and Computer Assisted Intervention – MICCAI 2021, Cham, 14–24,
693 https://doi.org/10.1007/978-3-030-87193-2_2, 2021.

694 Zhao, Z., Xu, G., Qi, Y., Liu, N., and Zhang, T.: Multi-patch deep features for power line insulator status classification
695 from aerial images, in: 2016 International Joint Conference on Neural Networks (IJCNN), 2016 International Joint
696 Conference on Neural Networks (IJCNN), 3187–3194, <https://doi.org/10.1109/IJCNN.2016.7727606>, 2016.

697 Zheng, Y., Rosenfeld, D., Zhu, Y., and Li, Z.: Satellite-Based Estimation of Cloud Top Radiative Cooling Rate for
698 Marine Stratocumulus, *Geophys. Res. Lett.*, 46, 4485–4494, <https://doi.org/10.1029/2019GL082094>, 2019.

699 Zhong, B., Chen, W., Wu, S., Hu, L., Luo, X., and Liu, Q.: A Cloud Detection Method Based on Relationship Between
700 Objects of Cloud and Cloud-Shadow for Chinese Moderate to High Resolution Satellite Imagery, *IEEE J. Sel. Top.*
701 *Appl. Earth Obs. Remote Sens.*, 10, 4898–4908, <https://doi.org/10.1109/JSTARS.2017.2734912>, 2017.

702 Zhu, W., Chen, T., Hou, B., Bian, C., Yu, A., Chen, L., Tang, M., and Zhu, Y.: Classification of Ground-Based Cloud
703 Images by Improved Combined Convolutional Network, *Appl. Sci.*, 12, 1570, <https://doi.org/10.3390/app12031570>,
704 2022.

705 Zhuo, W., Cao, Z., and Xiao, Y.: Cloud Classification of Ground-Based Images Using Texture–Structure Features, *J.*
706 *Atmospheric Ocean. Technol.*, 31, 79–92, <https://doi.org/10.1175/JTECH-D-13-00048.1>, 2014.

707